Extraction of near-surface properties from earthquake data recorded in a borehole using seismic interferometry

Kurang Mehta†, Roel Snieder† & Vladimir Graizer††
† *Center for Wave Phenomena, Department of Geophysics, Colorado School of Mines, Golden, CO 80401*
†† *California Strong Motion Instrumentation Program, Sacramento, CA 95814*

ABSTRACT

Seismic interferometry is a powerful tool in extracting the response of ground motion. We apply seismic interferometry for analysis of a magnitude 4.0 earthquake recorded by Treasure Island Geotechnical Array near San Francisco, California on 06/26/94. The focal depth of the event was 6.6 km and the epicenter was located at 12.6 km from the sensors in borehole. There were six 3-component sensors located at different depths. We deconvolve the waves recorded at different sensors to extract the coherent response of the near-surface from incoherent earthquake waves. Deconvolving the vertical component of the waveforms for each sensor with the sensor at the surface gives a superposition of an up- and a down-going wave whose velocity agrees with the P-wave velocity. Different time windows for the radial and the transverse components results in similar up- and down-going wave propagating with S-wave velocity. Deconvolution applied to the P-wave window of the radial component gives an up- and a down-going wave propagating with S-wave velocity. In the absence of any P to S conversion, the deconvolved waves should be travelling with the P-wave velocity. This suggests a P to S conversion at a depth below the deepest sensor. We use receiver functions, defined as the spectral ratio of the radial component with vertical component, to characterize the converted wave. In the receiver function, a P to S conversion is indicated by an arrival close to t=0 for the deepest sensor located at 104 m depth. We show the the waves obtained by deconvolution correspond to elements of the propagator matrix.

Key words: seismic interferometry, deconvolution, receiver function, propagator matrix

1 INTRODUCTION

Earthquake data recorded with sensors installed at different depths and geologic layers provide important information for studying local site effects (Graizer, et.al., 2004). We used an array of downhole sensors, known as the Treasure Island array (Shakal, et.al., 2004) to record ground motion data in the San Francisco Bay. The array was installed in 1992 in an area that experienced liquefaction during the Loma Prieta earthquake in 1989. Graizer et.al. (2004; 2000) analyzed these data to study site amplification effects as a function of depth. We show the usefulness of seismic interferometry, a technique based on combining signals recorded at different sensors, to characterize the near-surface information such as 1-D velocity profile and possible mode conversions.

Seismic interferometry is a powerful tool for extracting the impulse response of the ground motion from incoherent waveforms. This technique is usually based on cross-correlation of signal recorded at different receivers. The resulting signal represents the Green's function that characterizes the wave propagation between

the two receivers (Snieder, 2004; Snieder, et.al., 2006; Derode, et.al., 2003; Lobkis, et.al., 2001; Schuster, et.al., 2004; Wapenaar, 2004; Wapenaar, et.al., 2005; Shapiro, et.al., 2005; Shapiro, et.al., 2004). Elgamal et.al. (1995) demonstrated the use of cross-correlation on the Lotung seismic records to study the site dynamic response characteristics. In contrast, Snieder and Şafak (2006) applied deconvolution to extract the building response of the Robert A. Millikan Library in Pasadena, California. A different approach, known as normalized input-output minimization (NIOM), was developed by Kawakami and Haddidi (Kawakami, et.al., 1998; Haddadi, et.al.,1998a; Haddadi, et.al., 1998b) for extracting the impulse response of the ground motion and, hence, the physical properties of the soil layers. A similar analysis of wave propagation in buildings using the NIOM technique was carried out by Kawakami and Oyunchimeg (2003).

In this paper we show that by applying deconvolution to the incoherent waveforms excited by an earthquake, we retrieve the waves that propagate upward and downward along the array. These waves obtained by deconvolution can be used to estimate the 1-D velocity profile and mode conversion as discussed in the sections to follow. The paper is divided into three sections. Section 2 describes the data recorded by the Treasure Island array after an earthquake in 1994. The application of seismic interferometry to these data is shown in section 3. In the subsections of 3 we describe the waves obtained by deconvolving different components and the application of receiver function to downhole data to understand mode conversions.

The signal obtained by correlating two signals recorded at different receivers represents the Green's function that characterizes the wave propagation between the two receivers (Snieder, 2004; Snieder, et.al., 2006; Derode, et.al., 2003; Lobkis, et.al., 2001; Schuster, et.al., 2004; Wapenaar, 2004; Wapenaar, et.al., 2005; Shapiro, et.al., 2005; Shapiro, et.al., 2004). If instead of cross-correlating, the two signals are deconvolved, does the resulting signal also represent the Green's function? Section 4 addresses this question by establishing a connection between the up- and the down-going waves obtained by deconvolution and the propagator matrix elements.

2 EARTHQUAKE DATA RECORDED BY TREASURE ISLAND ARRAY

Downhole arrays of triaxial accelerometers have been instrumented throughout the state of California by the California Strong Motion Instrumentation Program (CSMIP). A geotechnical array, known as the Treasure Island array, was installed near San Francisco by CSMIP in co-operation with other agencies (Graizer, et.al., 2000). This array was installed to understand the response of soft-sediments to ground motion (Graizer, et.al., 2004). The array recorded waveforms excited by an earthquake on 06/26/94 at 08:42:50.31 (UTC). The earthquake occurred near Richmond, CA and hence, in this paper, is referred to as the Richmond earthquake. It was a 4.0 magnitude earthquake with focal depth of 6.6 km and epicenter 12.6 km from the sensors in borehole. The downhole array has six 3-component sensors located at different depths with the deepest one at a depth of 104 m. Each of the sensors is located in a different borehole separated by a horizontal distance of 10 ft. Figure 1 shows the radial component of the raw data. The data shows initial compressional waves (P-waves) followed by shear waves (S-waves) and surface waves arriving at later times. In this paper, we restrict our analysis to the body waves.

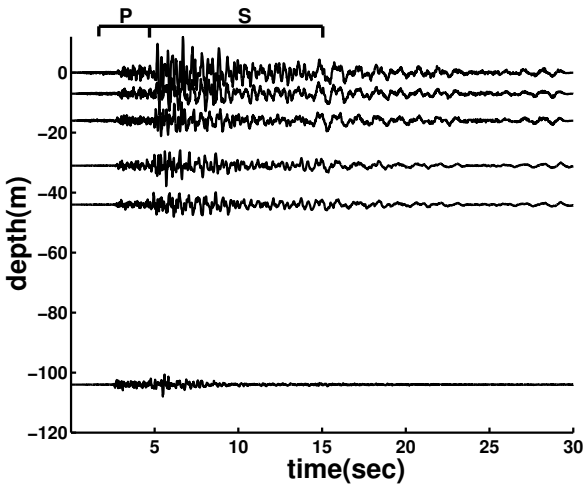

Figure 1. Radial component of the ground motion recorded by the Treasure Island array near San Francisco during the Richmond earthquake in 1994. The array consists of six 3-component sensors located at depths of 0, 7, 16, 31, 44, 104 m. The hypocenter of the earthquake is located at a depth of 6.6 km and a horizontal distance of 12.6 km from the downhole array of sensors. The time windows that is used for gating the P-waves (1.0 to 4.5 seconds) and the S-waves (4.5 to 15.0 seconds) is shown on the top.

3 SEISMIC INTERFEROMETRY USING DECONVOLUTION

We demonstrate the use of deconvolution as a tool for analyzing the earthquake data recorded by the Treasure Island Array. The deconvolution of two signals $A(\omega)$ and $B(\omega)$ in the frequency domain is given by

$$D(\omega) = \frac{A(\omega)}{B(\omega)}. \tag{1}$$

The deconvolution has poles at the zeros of the spectrum of $B(\omega)$. To avoid this instability, we perform a regularized deconvolution given by

$$D(\omega) = \frac{A(\omega)B^*(\omega)}{|B(\omega)|^2 + \epsilon}, \quad (2)$$

where the asterisk denotes complex conjugate and " ϵ " refers to the white-noise added at the denominator to prevent the instability of the equation 1.

For the Richmond earthquake data, we deconvolve the waveforms recorded at each of the sensors with the waveforms recorded by the sensor on the surface. The data recorded by Treasure Island array is multi-component, and hence we apply deconvolution to the transverse, the vertical and the radial component. Since we have both the radial and the vertical component at each of the sensors, we also generate the receiver function (Phinney. 1964; Wilson, et.al., 2003; Wilson, et.al., 2005a; Wilson, et.al., 2005b; Gilbert, et.al., 2003; Clouser, et.al., 1995; Dueker, et.al., 1997; Dueker, et.al., 1998; Langston, 1977; Li, et.al., 2000; Ramesh, et.al., 2002; Sheehan, et.al., 1995; Ammon, 1991) at each of the sensor locations to understand possible mode conversions. For the analysis of the three components, we apply deconvolution to the P- and the S-waves separately. Figure 1 shows the time windows we use for gating the P-waves (1.0 to 4.5 seconds) and the S-waves (4.5 to 15.0 seconds) before applying seismic interferometry.

3.1 Transverse component

Figure 2 shows the transverse component of the waveforms after deconvolving the waves in the S-wave window of the transverse component at each level with the waves in the S-wave window of the transverse component at the surface. The deconvolved waves show an up- and a down-going wave. Graizer et.al. (2004) show the 1-D profile of the P-wave velocity and the S-wave velocity at the Treasure Island array location. The two methods used for generating their 1-D velocity profile are suspension logging and classical downhole measurements (performed by the USGS). We show the travel-time curve (dashed line) for up- and down-going S-waves inferred from their model. Different slopes of the travel-time curve at different depths are due to changes in the shear velocity at these depths. The agreement of the travel-time curve with the wave-propagation obtained by deconvolving the waves suggests that deconvolution as a tool for seismic interferometry can be used for extracting the impulse response from incoherent recording of the ground motion. This makes it possible to estimate the 1-D velocity profile.

Deconvolution of the waves in the S-wave window at different sensors with the waves in the S-wave window at the surface can, thus, be used to estimate the 1-D velocity profile of the S-waves. If, instead of using the S-wave window, the deconvolution is applied to the transverse component with the waves in the P-wave window, the resulting signal is shown in Figure 3. Given that the transverse component does not carry significant P-wave information, the deconvolved signal at the surface is a spike whereas the deconvolved signal at the deeper sensors does not show any meaningful wave propagation.

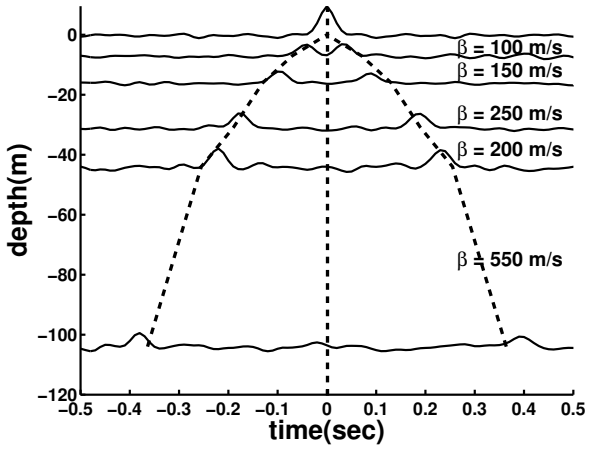

Figure 2. Up- and down-going waves obtained by deconvolving the waves in the S-wave window of the transverse component at each sensor location with the waves in the S-wave window of the transverse component at the surface. The dashed lines show the travel-time curve of the up- and down-going S-waves obtained from the S-wave velocity profile.

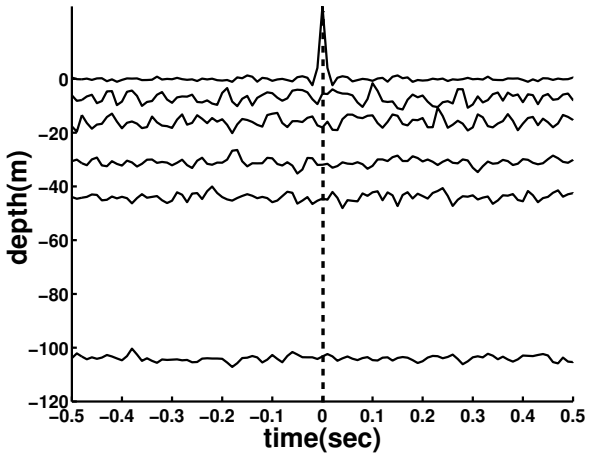

Figure 3. Waveforms obtained by deconvolving the waves in the P-wave window of the transverse component at each sensor location with the waves in the P-wave window of the transverse component at the surface. Note the lack of coherent up- and down-going waves.

3.2 Vertical component

For the vertical component, we apply deconvolution to the waves in the time window that includes both P- and S-waves. Figure 4 shows the waveforms after deconvolving the waves recorded at each of the sensors with the waves recorded at the sensor on the surface. Similar to Figure 2, there is an up- and a down-going

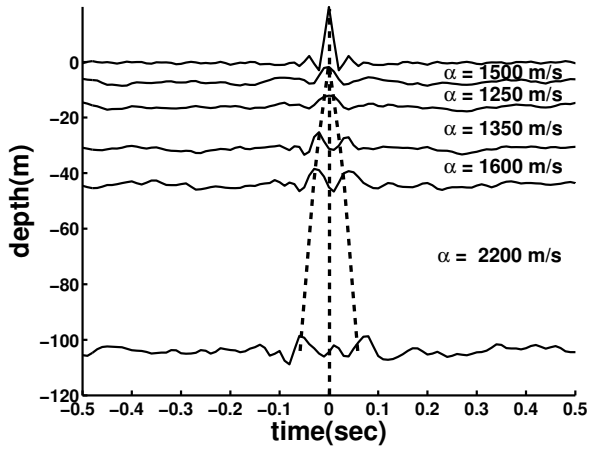

Figure 4. Up- and down-going waves obtained by deconvolving the waves recorded by the vertical component at each sensor location with the waves recorded by vertical component at the surface. The dashed lines show the travel-time curve of the up- and down-going P-waves obtained from the P-wave velocity profile.

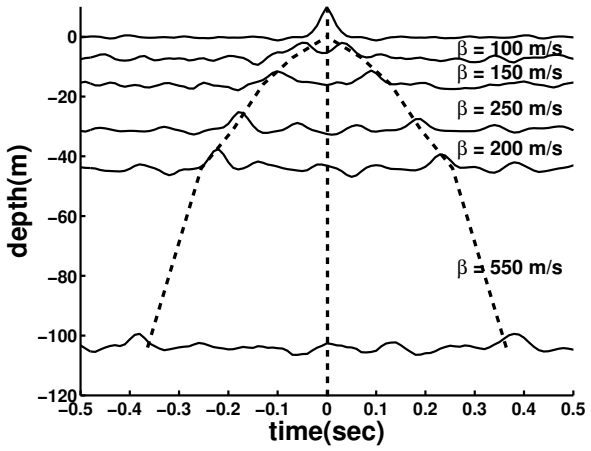

Figure 5. Up- and down-going waves obtained by deconvolving the waves in the S-wave window of the radial component at each sensor location with the waves in the S-wave window of the radial component at the surface. The dashed lines show the travel-time curve of the up- and down-going S-waves obtained from the S-wave velocity profile.

wave that propagates with a higher velocity than the deconvolved waves in Figure 2. We show the travel-time curve (dashed line) for up- and down-going P-waves inferred from this model using the 1-D velocity profile for P-waves. The travel-time curve agrees with the up- and the down-going wave obtained by deconvolution. Hence, deconvolution of the vertical component gives an up- and a down-going wave, that can be used to an estimate of the 1-D velocity profile of the P-waves.

3.3 Radial component

Deconvolution of the waves recorded by the radial component at each of the sensors with the waves recorded at the sensor on the surface also results in an up- and a down-going wave. When only the waves in the S-wave window are used for deconvolution, it results in an up- and a down-going S-wave as shown in Figure 5. The dashed line representating the S-wave travel-time curve agrees well with these up- and down-going waves.

If we apply deconvolution to the waves in the P-wave window, we would expect to retrieve the up- and down-going P-waves. Surprisingly, Figure 6 shows that if we deconvolve the waves in the P-wave window of the radial component, the resultant waves propagate with S-wave velocity. One possible explanation to this interesting result is that there is a P to S conversion at a depth below the downhole array and hence the arrivals before the primary S-wave in Figure 1 contain S-waves generated by P to S conversion. To diagnose this P to S conversion, we use receiver function.

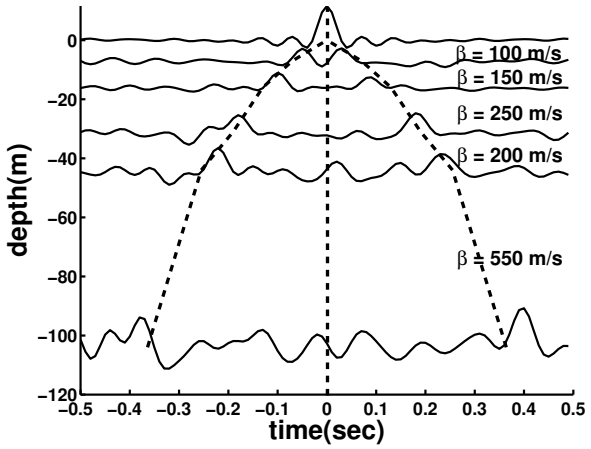

Figure 6. Up- and down-going waves obtained by deconvolving the waves in the P-wave window of the radial component at each sensor location with the waves in the P-wave window of the radial component at the surface. Interestingly, the propagating waves agree with the dashed line representating the travel-time curve of the S-waves obtained from the S-wave velocity profile.

3.4 Receiver Function

Receiver function (Phinney. 1964; Wilson, et.al., 2003; Wilson, et.al., 2005a; Wilson, et.al., 2005b; Gilbert, et.al., 2003; Clouser, et.al., 1995; Dueker, et.al., 1997; Dueker, et.al., 1998; Langston, 1977; Li, et.al., 2000; Ramesh, et.al., 2002; Sheehan, et.al., 1995; Ammon, 1991), defined as the spectral ratio of the radial component and the vertical component, can be used to characterize the converted waves. We show the application of receiver functions to borehole data to detect P to S con-

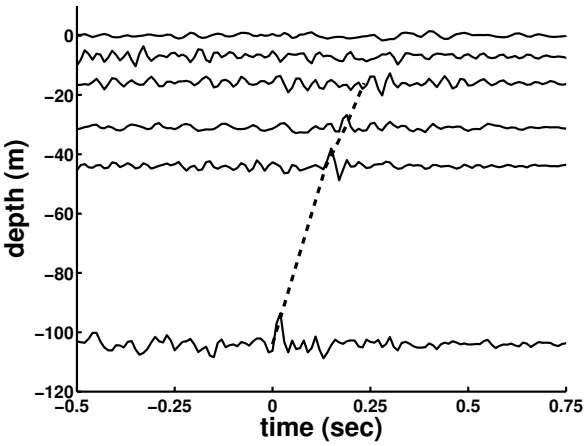

Figure 7. Receiver function, defined as the spectral ratio of the data recorded by the radial component with the data recorded by the vertical component at the same level. Each of the traces represent the spectral ratio of the radial component at that specific sensor with the data recorded at the corresponding vertical component. The up-going wave agrees with the travel-time curve (shown in dashed line) for a P to S converted wave with the conversion point just below the deepest sensor.

verted waves. We define receiver function in a borehole as the spectral ratio of the radial component recorded at each of the sensor location in a borehole and the vertical component at the same sensor location. In other words, it is deconvolution of the waves recorded by the radial component at each of the sensor location with the waves recorded by the vertical component at the same sensor location. Figure 7 shows that the receiver function at every sensor location results in an up-going wave. Since the propagating pulse is close to time t=0 at the deepest sensor (104 m), the conversion occurs at a depth just below the deepest sensor. The dashed line indicates the travel-time curve of the converted wave calculated, using the P- and the S-wave velocity from Graizer et.al. (2004), assuming a P to S conversion. The agreement of the up-going wave and this travel-time curve suggests that the receiver function applied to this earthquake data (recorded in a borehole) gives an up-going converted wave. This supports the observation that there is a P to S conversion just below the downhole array.

4 ANALYSIS WITH PROPAGATOR MATRIX

The signal obtained by correlating two waveforms recorded at different receivers represents the Green's function that characterizes the wave propagation between the two receivers (Snieder, 2004; Snieder, et.al., 2006; Derode, et.al., 2003; Lobkis, et.al., 2001; Schuster, et.al., 2004; Wapenaar, 2004; Wapenaar, et.al., 2005; Shapiro, et.al., 2005; Shapiro, et.al., 2004). However, if the two signals are deconvolved, as in our analysis of the Richmond earthquake data, does the resulting signal also represent the Green's function? The Richmond earthquake data is recorded by vertically separated sensors and the waveforms recorded at each of the sensors is deconvolved with the waveforms recorded at the sensor on the surface. Here we establish the connection between the up- and the down-going waves obtained by deconvolution and propagator matrix analysis for SH waves by Trampert et.al.(1993). For a general layered medium with one of the sensors in a borehole (depth z) and another one at the free surface, the displacement and stress values for a SH wave at a depth z is expressed as matrix multiplication of the propagator matrix with the displacement and stress values at the free surface (z=0) (Aki, et.al., 2002). Since the traction at the free surface is zero, this matrix multiplication can be written as

$$\begin{pmatrix} u_y(z,\omega) \\ \sigma_{yz}(z,\omega) \end{pmatrix} = P^{SH}(z,0;\omega) \begin{pmatrix} u_y(0,\omega) \\ 0 \end{pmatrix}. \qquad (3)$$

This is a system of two equations. The first equation can be solved for the SH propagator matrix element as

$$P_{11}^{SH}(z,0;\omega) = \frac{u_y(z,\omega)}{u_y(0,\omega)}. \qquad (4)$$

For SH waves, deconvolution of the waveforms recorded at a depth with the waveforms recorded at the surface thus gives the P_{11} element of the propagator matrix (Trampert, et.al., 1993). Does this also hold true for the PSV waves? To answer this question we consider the frequency domain analysis using propagator matrices by van Vossen et.al. (2004) Since one of the sensors is at the free surface, the tractions at that sensor vanish. Using this property, they combine the PSV (4*4) and SH (2*2) propagator matrix to give

$$\begin{pmatrix} u_x(z,\omega) \\ u_y(z,\omega) \\ u_z(z,\omega) \end{pmatrix} = P(z,0;\omega) \begin{pmatrix} u_x(0,\omega) \\ u_y(0,\omega) \\ u_z(0,\omega) \end{pmatrix} \qquad (5)$$

where

$$P(z,0;\omega) \quad = \quad \begin{pmatrix} P_{11}^{PSV} & 0 & iP_{12}^{PSV} \\ 0 & P_{11}^{SH} & 0 \\ -iP_{21}^{PSV} & 0 & P_{22}^{PSV} \end{pmatrix}. \qquad (6)$$

$P_{ij}^{PSV/SH}$ stands for ij-element of the $PSV_{(4*4)}$ or $SH_{(2*2)}$ propagator matrix. A derivation of combining the PSV and the SH propagator matrices to give equation 6 is shown in Appendix A. Since all the following expressions in this paper are in frequency domain, we drop the ω for the rest of the paper and denote the propagator matrix as $P(z,0)$ instead of $P(z,0;\omega)$.

We show in Appendix B the analysis by van Vossen et.al. (2004) to express the propagator matrix elements in the measured displacements. The analysis of van Vossen et.al. (2004) is, however, limited to lossless media. We extend this analysis to lossy media for a special

case of attenuative media for waves with normal incidence. In the presence of attenuation (Johnston, et.al., 1981) the expression for the components of the propagator matrix can be expressed as (Aki, et.al., 2002)

$$\begin{aligned} P_{11}^{SH}(z,0) &= \exp[i\omega q_s z - \xi_s z] + \exp[-i\omega q_s z + \xi_s z] \\ &= 2\cos[(\omega q_s + i\xi_s)z], \end{aligned} \tag{7}$$

$$\begin{aligned} P_{11}^{PSV}(z,0) &= 2\beta^2 p^2[\cos\omega q_p z \cosh\xi_p z \\ &- i\sin\omega q_p z \sinh\xi_p z] + (1-2\beta^2 p^2) \\ &[\cos\omega q_s z \cosh\xi_s z \\ &- i\sin\omega q_s z \sinh\xi_s z] \\ &= 2\beta^2 p^2 \cos[(\omega q_p + i\xi_p)z] + (1-2\beta^2 p^2) \\ &\cos[(\omega q_s + i\xi_s)z], \end{aligned} \tag{8}$$

$$\begin{aligned} iP_{12}^{PSV}(z,0) &= \frac{p}{q_p}(1-2\beta^2 p^2)[\cos\omega q_p z \sinh\xi_p z \\ &- i\sin\omega q_p z \cosh\xi_p z] - 2\beta^2 p q_s \\ &[\cos\omega q_s z \sinh\xi_s z - i\sin\omega q_s z \cosh\xi_s z] \\ &= \frac{-ip}{q_p}(1-2\beta^2 p^2)\sin[(\omega q_p + i\xi_p)z] \\ &+ 2i\beta^2 p q_s \sin[(\omega q_s + i\xi_s)z], \end{aligned} \tag{9}$$

$$\begin{aligned} -iP_{21}^{PSV}(z,0) &= \frac{-p}{q_s}(1-2\beta^2 p^2)[\cos\omega q_s z \sinh\xi_s z \\ &- i\sin\omega q_s z \cosh\xi_s z] - 2\beta^2 p q_p \\ &[\cos\omega q_p z \sinh\xi_p z - i\sin\omega q_p z \cosh\xi_p z] \\ &= \frac{ip}{q_s}(1-2\beta^2 p^2)\sin[(\omega q_s + i\xi_s)z] \\ &- 2i\beta^2 p q_p \sin[(\omega q_p + i\xi_p)z], \end{aligned} \tag{10}$$

$$\begin{aligned} P_{22}^{PSV}(z,0) &= 2\beta^2 p^2[\cos\omega q_s z \cosh\xi_s z \\ &- i\sin\omega q_s z \sinh\xi_s z] + (1-2\beta^2 p^2) \\ &[\cos\omega q_p z \cosh\xi_p z \\ &- i\sin\omega q_p z \sinh\xi_p z] \\ &= 2\beta^2 p^2 \cos[(\omega q_s + i\xi_s)z] \\ &+ (1-2\beta^2 p^2)\cos[(\omega q_p + i\xi_p)z], \end{aligned} \tag{11}$$

where ω is the angular frequency, β the S-wave velocity, p the horizontal slowness, q_p the vertical slowness for P-waves, q_s the vertical slowness for S-waves, ξ_p the imaginary part of the vertical wavenumber for P-waves, and ξ_s the imaginary part of the vertical wavenumber for S-waves.

In general, all the propagator matrix elements are complex. However, for the lossless case, P_{11}^{PSV}, P_{11}^{SH} and P_{22}^{PSV} are real and P_{12}^{PSV} and P_{21}^{PSV} are imaginary. We show in Appendix B how equation 5 can be solved for the propagator matrix elements. For the lossy case, the system is underdetermined and hence needs more information to express elements of the propagator matrix in the measured displacement. An important parameter in the expressions of the propagator matrix elements is the horizontal slowness p which depends on the angle of incidence. Using the velocity structure of the subsurface up to the hypocenter of the earthquake (Wald, et.al., 1991), we show in Figure 8 the angle of incidence as a function of the depth. Figure 8 implies that the waves arrive at the surface at near-normal incidence (4°). For normal incidence ($\theta \approx 0°$), the cross-terms P_{12}^{PSV} and P_{21}^{PSV} in the propagator matrix goes to zero.

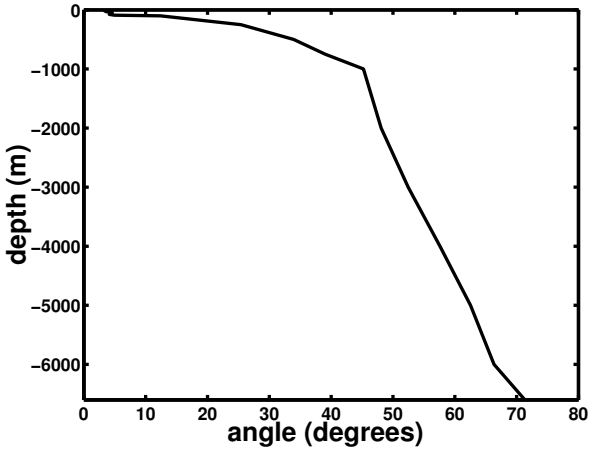

Figure 8. Angle of incidence as a function of depth.

$$\begin{aligned} &P_{12}^{PSV}(z,0) = 0, \\ &P_{21}^{PSV}(z,0) = 0. \end{aligned} \tag{12}$$

Substituting equation 12 into equation 5 gives the simplified linear system of equations:

$$\begin{aligned} u_x(z,\omega) &= P_{11}^{PSV}(z,0)u_x(0,\omega), \\ u_y(z,\omega) &= P_{11}^{SH}(z,0)u_y(0,\omega), \\ u_z(z,\omega) &= P_{22}^{PSV}(z,0)u_z(0,\omega). \end{aligned} \tag{13}$$

Solving the system of equation in 13 gives the propagator elements in terms of displacements:

$$\begin{aligned} P_{11}^{SH}(z,0) &= \frac{u_y(z,\omega)}{u_y(0,\omega)}, \\ P_{11}^{PSV}(z,0) &= \frac{u_x(z,\omega)}{u_x(0,\omega)}, \\ P_{22}^{PSV}(z,0) &= \frac{u_z(z,\omega)}{u_z(0,\omega)}. \end{aligned} \tag{14}$$

The first equation is the same as equation 4. The other two equations show that even for the PSV waves, we can obtain the propagator matrix elements by applying deconvolution. This also holds true for an attenuative medium in a special case of normal incidence. For the Treasure Island data, we perform deconvolution to get the up- and down-going waves and equation 14 shows these deconvolved waves correspond to

the propagator matrix elements. In this analysis, one of the sensors is always at the free surface because of which traction vanishes at that sensor location. If instead the waves recorded at a given depth are deconvolved with the waves recorded at a different depth ($z \neq 0$), the traction values are non-zero and become a part of the analysis.

This analysis is valid for a homogeneous medium. For a layered medium, the propagator matrix in equation 13 can be obtained by combining the PSV and SH propagator matrices, each of which is the product of the corresponding propagator matrices for each of the layers. These product matrices can be combined as shown in Appendix A. If each of the layers are homogeneous, the resultant matrix is still diagonal and hence, applying deconvolution to the waveforms recorded in a layered medium results in the propagator matrix elements of the matrix obtained by combining the PSV and the SH matrix of the layered medium.

5 DISCUSSION

An important point of discussion is the use deconvolution as opposed to cross-correlation for seismic interferometry. The wavefield obtained from cross-correlation is, in the frequency domain, the product of the wavefield obtained by deconvolution and the power spectrum of the wavefield at the target level. The wavefield at the target level refers to the wavefield used in the denominator while performing deconvolution. If the power spectrum of the target level wavefield is white, the wavefield obtained by correlation is the same as the wavefield obtained by deconvolution, scaled by the power spectrum. For a target level with a non-white power spectrum, however, correlation gives wavefield that is the product of the wavefield obtained by deconvolution and the frequency dependent target level power spectrum. So, depending on the power spectrum of the wavefield at the target level, we can use deconvolution or cross-correlation.

Apart from getting the impulse response and hence the 1-D velocity profile, the deconvolved waveforms can also be used to study the lateral variations in the velocity structure. In Figures 2-6, showing the deconvolved waves, a vertical dashed line indicates zero time. In the absence of lateral variations in the velocity, the waveforms for negative times would be, kinematically, the mirror image of the waveforms recorded for positive times. We do not observe the mirror symmetry in the deconvolved waveforms. This indicates that there could be lateral variations in the velocity. The lack of mirror symmetry could be due to other reasons such as dipping layers, sensors placed in different boreholes and anisotropy.

We established a connection between the up- and down-going waves and the propagator matrix elements. For the analysis using propagator matrix we assume normal incidence. We also show, using receiver functions, that there is a P to S conversion. However, for normal incidence and a horizontally layered structure there are no mode conversions. The angle of incidence as a function of depth (Figure 8) shows that the incidence angle at the surface is $\approx 4^\circ$. Since the incidence is not strictly normal, there could be mode conversions like the one we show using receiver functions.

6 CONCLUSION

We show the use of deconvolution as a tool for seismic interferometry, for data recorded by the Treasure Island array, resulting in a superposition of up- and down-going waves. This makes it a valuable tool in estimating the 1-D velocity profile along the recording array. Application of deconvolution to various components of the data results in waves either propagating with P- or S-wave velocity, and depends on the time window used for gating before applying deconvolution. For both the transverse and radial components, deconvolution of the waves in the S-wave window results in the up- and down-going waves with S-wave velocity. Deconvolution applied to the vertical component results in up- and down-going waves with the P-wave velocity. Interestingly, the waves in the P-wave window of the radial component, when deconvolved, results in waves propagating with the S-wave velocity. We use the receiver functions applied to data in a downhole to show a P to S conversion just below the deepest sensor. Finally, we establish a connection of the resultant up- and down-going waves with the propagator matrix elements and show that this type of analysis is possible even in the presence of attenuation as long as we restrict ourselves to normal incidence.

ACKNOWLEDGMENTS

We thank the support provided by the sponsors of the Consortium Project on Seismic Inverse Methods for Complex Structures at the Center for Wave Phenomena. We also thank the financial support provided by the Gamechanger program of Shell International Exploration and Production Inc. We appreciate the critical comments from John Stockwell and Steve Smith.

REFERENCES

Aki, K., and P. G. Richards, "Quantitative Seismology," University Science Books, Sausalito, 2nd edition (2002).

Ammon, C. J., "The isolation of receiver effects from teleseismic P waveforms," Bulletin of Seismological Society of America, **81**, No. 6., 2504-2510 (1991).

Clouser, R. H., and C. A. Langston, "Effect of sinusoidal interfaces on teleseismic P-wave receiver functions," Geophysics Journal International, **123**, 541-558 (1995).

Derode, A., E. Lacrose, M. Campillo, and M. Fink, "How to estimate the Green's function for a heterogeneous medium between two passive sensors? Application to acoustic waves," Applied Physics Letters, **83**, 3054-3056 (2003).

Dueker, K. G. and A. F. Sheehan, "Mantle discontinuity structure from midpoint stacks of converted P to S waves across the Yellowstone hotspot track," Journal of Geophysical Research, **102**, 8313-8327 (1997).

Dueker, K. G., and A. F. Sheehan, "Mantle discontinuity structure beneath the Colorado Rocky Mountains and High Plains," Journal of Geophysical Research, **103**, 7153-7169 (1998).

Langston, C. A., "Corvallis, Oregon, crustal and upper mantle receiver structure from teleseismic P-waves and S-waves," Bulletin of Seismological Society of America, **67**, 713-724 (1977).

Gilbert, H. J., A. F. Sheehan, K. G. Dueker, and P. Molnar, "Receiver functions in the western United States, with implications for upper mantle structure and dynamics," Journal of Geophysical Research, **108**, (B5), 2229, doi:10.1029/2001JB001194 (2003).

Graizer, V., T. Cao, A. Shakal, and P. Hipley, "Data from downhole arrays instrumented by the California Strong Motion Instrumentation Program in studies of site amplification effects,"Proceedings of the 6th International Conference on Seismic Zonation, 2000, Palm Springs, California.

Graizer, V., and A. Shakal, "Analysis of some of CSMIP strong-motion geotechnical array recordings," Proceedings of the International Workshop for Site Selection, Installation and Operation of Geotechnical Strong-Motion Arrays: Workshop 1, Inventory of Current and Planner Arrays. 14 and 15 October 2004. COSMOS, SCEC and USC.

Haddadi, H. R., and H. Kawakami, "Modeling wave propagation by using normalized input-output minimization (NIOM) method for multiple linear systems," Journal of Structural, Mechanical and Earthquake Engineering, **15**, No. 1, 29s-39s (1998a).

Haddadi, H. R., and H. Kawakami, "Characteristics of Vertical Component Strong Ground Motion by NIOM (Normalized Input-Output Minimization) Method," Proceedings of 10th Japan Symposium of Earthquake Engineering, 1187-1192 (1998b).

Johnston D. H., and M. N. Toksöz, "Definitions and Terminology," Geophysics Reprint Series No.2, Seismic Wave Attenuation, 1-5 (1981).

Kawakami, H., and H. R. Haddadi, "Modeling wave propagation by using normalized input-output minimization (NIOM)," Soil Dynamics and Earthquake Engineering, **17**, 117-126 (1998).

Kawakami, H., and M. Oyunchimeg, "Normalized input-output minimization analysis of wave propagation in buildings," Engineering Structures, **25**, 1429-1442 (2003).

Li, X., S. V. Sobolev, R. Kind, X. Yuan, and C. Estabrook, "A detailed receiver function image of the upper mantle discontinuities in the Japan subduction zone," Earth and Planetary Science Letters, **183**, 527-541 (2000).

Lobkis, O. I., and R. L. Weaver, "On the emergence of the Green's function in the correlations of a diffuse field," Journal of Acoustical Society of America, **110**, 3011-3017 (2001).

Phinney, R. A., "Structure of the Earth's Crust from Spectral Behavior of Long-Period Body Waves," Journal of Geophysical Research, **69**, No. 14, 2997-3017 (1964).

Ramesh, D. S., R. Kind, and X. Yuan, "Receiver function analysis of the North American crust and upper mantle," Geophysics Journal International, **150**, 91-108 (2002).

Schuster, G. T., J. Yu, J. Sheng, and J. Rickett, "Interferometric/daylight seismic imaging," Geophysics Journal International, **157** 838-852 (2004).

Shakal, A., P. Hipley, and V. Graizer, "CSMIP Instrumented Geotechnical Arrays,"Proceeding of the International Workshop for Site Selection, Installation and Operation of Geotechnical Strong-Motion Arrays: Workshop 1, Inventory of Current and Planned Arrays. 14 and 14 October 2004, Los Angeles.

Shapiro, N. M., and M. Campillo, "Emergence of broadband Rayleigh waves from correlations of the ambient seismic noise," Geophysics Research Letters, **31**, L07614, doi10.1029/2004GL019491 (2004).

Shapiro, N. M., M. Campillo, L. Stehly, and M. H. Ritzwoller, "High-resolution surface-wave tomography from ambient seismic noise," Science, **307**, 1615-1618 (2005).

Sheehan, A. F., G. A. Abers, C. H. Jones, and A. L. Lerner-Lam, "Crustal thickness variations across the Colorado Rocky Mountains from teleseismic receiver functions," Journal of Geophysical Research, **100**, 20391-20404 (1995).

Snieder, R., "Extracting the Green's function from the correlation of coda waves: A derivation based on stationary phase," Physics Review E., **69**, 046610 (2004).

Snieder, R., and E. Şafak, "Extracting the building response using seismic interferometry; theory and application to the Millikan Library in Pasadena, California," Bulletin of Seismological Society of America, **96**, No. 2, 586-598 (2006).

Snieder, R., K. Wapenaar, and K. Larner, "Spurious multiples in interferometric imaging of primaries," Geophysics, in Press (2006).

Trampert, J., M. Cara, and M. Frogneux, "SH propagator matrix and Q_s estimates from borehole- and surface-recorded earthquake data," Geophysics Journal International, **112**, 290-299 (1993).

van Vossen, R., J. Trampert and A. Curtis, "Propagator and wave-equation inversion for near-receiver material properties," Geophysical Journal International, **157**, 796-812 (2004).

Wald, D. J., D. V. Helmberger, and T. H. Heaton, "Rupture Model of the 1989 Loma Prieta earthquake from the inversion of strong-motion and broadband teleseismic data," Bulletin of the Seismological Society of America, **81**, No. 5, 1540-1572 (1991).

Wapenaar, K., "Retrieving the elastodynamic Green's function of an arbitrary inhomogeneous medium by cross-correlation," Physics Review Letters, **93**, 254301 (2004).

Wapenaar, K., J. Fokkema, and R. Snieder, "Retrieving the Green's function by cross-correlation: a comparison of approaches," Journal of Acoustical Society of America, **118**, 2783-2786 (2005).

Wilson, D., and R. Aster, "Imaging crust and upper mantle seismic structure in the southwestern United States using teleseismic receiver functions," The Leading Edge, 232-237 (2003).

Wilson, D., and R. Aster, "Seismic imaging of the crust and upper mantle using regularized joint receiver functions, frequency-wave number filtering, and multimode Kirchoff migration," Journal of Geophysical Research, **110**, B05305, doi:10.1029/2004JB003430 (2005a).

Wilson, D., R. Aster, J. Ni, S. Grand, M. West, W. Gao, W. S. Baldridge, and S. Semken, "Imaging the seismic structure of the crust and upper mantle beneath the Great Plains, Rio Grande Rift, and Colorado Plateau using receiver functions," Journal of Geophysical Research, **110**, B05306, doi:10.1029/2004JB003492 (2005b).

APPENDIX A: DERIVATION OF THE PROPAGATOR MATRIX

The displacement and stress values for a SH wave at a depth z can be expressed as matrix multiplication of the propagator matrix and the values at the free surface (z=0) (Aki, et.al., 2002). Since the traction at the free surface is zero, we can write the multiplication as

$$\begin{pmatrix} u_y(z,\omega) \\ \sigma_{yz}(z,\omega) \end{pmatrix} = P^{SH}(z,0) \begin{pmatrix} u_y(0,\omega) \\ 0 \end{pmatrix} \tag{A1}$$

$$\Rightarrow u_y(z,\omega) = P_{11}^{SH}(z,0) u_y(0,\omega). \tag{A2}$$

A similar expression for the PSV system is given by

$$\begin{pmatrix} u_x(z,\omega) \\ iu_z(z,\omega) \\ \sigma_{xz}(z,\omega) \\ i\sigma_{zz}(z,\omega) \end{pmatrix} = P^{PSV}(z,0) \begin{pmatrix} u_x(0,\omega) \\ iu_z(0,\omega) \\ 0 \\ 0 \end{pmatrix}, \tag{A3}$$

hence

$$\begin{aligned} u_x(z,\omega) &= P_{11}^{PSV}(z,0) u_x(0,\omega) \\ &+ iP_{12}^{PSV}(z,0) u_z(0,\omega), \\ iu_z(z,\omega) &= P_{21}^{PSV}(z,0) u_x(0,\omega) \\ &+ iP_{22}^{PSV}(z,0) u_z(0,\omega). \end{aligned} \tag{A4}$$

Equations A2 and A4 can be combined to the following system of equations:

$$\begin{aligned} u_y(z,\omega) &= P_{11}^{SH}(z,0) u_y(0,\omega), \\ u_x(z,\omega) &= P_{11}^{PSV}(z,0) u_x(0,\omega) \\ &+ iP_{12}^{PSV}(z,0) u_z(0,\omega), \\ u_z(z,\omega) &= -iP_{21}^{PSV}(z,0) u_x(0,\omega) \\ &+ P_{22}^{PSV}(z,0) u_z(0,\omega). \end{aligned} \tag{A5}$$

This system of equations can be re-written in matrix form as

$$\begin{pmatrix} u_x(z,\omega) \\ u_y(z,\omega) \\ u_z(z,\omega) \end{pmatrix} = P(z,0) \begin{pmatrix} u_x(0,\omega) \\ u_y(0,\omega) \\ u_z(0,\omega) \end{pmatrix}, \tag{A6}$$

where

$$P(z,0) = \begin{pmatrix} P_{11}^{PSV} & 0 & iP_{12}^{PSV} \\ 0 & P_{11}^{SH} & 0 \\ -iP_{21}^{PSV} & 0 & P_{22}^{PSV} \end{pmatrix} \tag{A7}$$

is the propagator matrix relating the displacements at a depth z with the displacements at the free surface (z=0). This holds in general for any layered elastic medium provided one of the sensors is at the free surface.

APPENDIX B: SOLVING FOR THE PROPAGATOR MATRIX ELEMENTS IN TERMS OF DISPLACEMENTS

For the solution of the propagator matrix elements, we restrict the analysis to homogeneous medium. The following expressions for the elements of SH and PSV matrices are obtained from Aki and Richards (2002) and are simplified to agree with the expressions given by van Vossen et.al. (2004),

$$\begin{aligned} P_{11}^{SH}(z,0) &= 2\cos(i\nu z) \\ &= 2\cos(\omega q_s z), \end{aligned} \tag{B1}$$

$$\begin{aligned} P_{11}^{PSV}(z,0) &= 1 + \frac{2\mu}{\omega^2\rho}\left[2k^2 \sinh^2\left(\frac{\gamma z}{2}\right)\right. \\ &- \left.(k^2+\nu^2)\sinh^2\left(\frac{\nu z}{2}\right)\right] \\ &= 2\beta^2 p^2 \cos(\omega q_p z) + (1 - 2\beta^2 p^2) \\ &\quad \cos(\omega q_s z), \end{aligned} \tag{B2}$$

$$\begin{aligned} P_{12}^{PSV}(z,0) &= \left(\frac{k\mu}{\omega^2\rho}\right)(k^2+\nu^2)\left(\frac{\sinh\gamma z}{\gamma}\right) \\ &- \left(\frac{2k\mu}{\omega^2\rho}\right)(\nu \sinh\nu z) \\ &= \left(\frac{-p(1-2\beta^2p^2)}{q_p}\right)\sin(\omega q_p z) \\ &+ 2\beta^2 p q_s \sin(\omega q_s z) \\ \Rightarrow iP_{12}^{PSV}(z,0) &= \frac{-ip}{q_p}(1-2\beta^2p^2)\sin(\omega q_p z) \\ &+ 2i\beta^2 p q_s \sin(\omega q_s z), \end{aligned} \tag{B3}$$

$$\begin{aligned} P_{21}^{PSV}(z,0) &= \left(\frac{k\mu}{\omega^2\rho}\right)(k^2+\nu^2)\left(\frac{\sinh\nu z}{\nu}\right) \\ &- \left(\frac{2k\mu}{\omega^2\rho}\right)(\gamma \sinh\gamma z) \\ \Rightarrow -iP_{21}^{PSV}(z,0) &= \frac{ip}{q_s}(1-2\beta^2p^2)\sin[\omega q_s z] \\ &- 2i\beta^2 p q_p \sin[\omega q_p z], \end{aligned} \tag{B4}$$

$$
\begin{aligned}
P_{22}^{PSV}(z,0) &= 1+\frac{2\mu}{\omega^2\rho}\left[2k^2\sinh^2\left(\frac{\nu z}{2}\right)\right. \\
&- \left.(k^2+\nu^2)\sinh^2\left(\frac{\gamma z}{2}\right)\right] \\
\Rightarrow P_{22}^{PSV}(z,0) &= 2\beta^2p^2\cos[\omega(q_s z)]+(1-2\beta^2p^2) \\
&\quad \cos[\omega(q_p z)], \qquad \text{(B5)}
\end{aligned}
$$

where ν is the vertical wavenumber for S-waves and γ is the vertical wavenumber for P-waves ($\nu = i\omega q_s$ and $\gamma = i\omega q_p$).

As shown by van Vossen et.al. (2004), for lossless medium, we can solve equation A6 for the components of the propagator matrix. To solve for the propagator matrix elements, we start with equation A6:

$$
\begin{pmatrix} u_x(z,\omega) \\ u_y(z,\omega) \\ u_z(z,\omega) \end{pmatrix} = P(z,0)\begin{pmatrix} u_x(0,\omega) \\ u_y(0,\omega) \\ u_z(0,\omega) \end{pmatrix}, \qquad \text{(B6)}
$$

where

$$
P(z,0) = \begin{pmatrix} P_{11}^{PSV} & 0 & iP_{12}^{PSV} \\ 0 & P_{11}^{SH} & 0 \\ -iP_{21}^{PSV} & 0 & P_{22}^{PSV} \end{pmatrix}.
$$

In absence of attenuation P_{11}^{PSV}, P_{11}^{SH} and P_{22}^{PSV} are real and P_{12}^{PSV} and P_{21}^{PSV} are imaginary. In order to solve for the propagator matrix elements, we equate the real and imaginary parts in equation B6 to give the following equations:

$$
\begin{aligned}
Re(u_x(z,\omega)) &= P_{11}^{PSV}(z,0)Re(u_x(0,\omega)) \\
&- P_{12}^{PSV}(z,0)Im(u_z(0,\omega)), \\
Im(u_x(z,\omega)) &= P_{11}^{PSV}(z,0)Im(u_x(0,\omega)) \\
&+ P_{12}^{PSV}(z,0)Re(u_z(0,\omega)), \\
Re(u_z(z,\omega)) &= P_{21}^{PSV}(z,0)Im(u_x(0,\omega)) \\
&+ P_{22}^{PSV}(z,0)Re(u_z(0,\omega)), \\
Im(u_z(z,\omega)) &= -P_{21}^{PSV}(z,0)Re(u_x(0,\omega)) \\
&+ P_{22}^{PSV}(z,0)Im(u_z(0,\omega)). \qquad \text{(B7)}
\end{aligned}
$$

Solving this system of equations for the elements of propagator matrix gives

$$
P_{11}^{SH}(z,0) = \frac{u_y(z,\omega)}{u_y(0,\omega)},
$$

$$
\begin{aligned}
P_{11}^{PSV}(z,0) &= \left(\frac{1}{R(\omega)}\right)[Re(u_x(z,\omega))Re(u_z(0,\omega)) \\
&+Im(u_x(z,\omega))Im(u_z(0,\omega))],
\end{aligned}
$$

$$
\begin{aligned}
P_{12}^{PSV}(z,0) &= \left(\frac{i}{R(\omega)}\right)[Re(u_x(0,\omega))Im(u_x(z,\omega)) \\
&-Im(u_x(0,\omega))Re(u_x(z,\omega))],
\end{aligned}
$$

$$
\begin{aligned}
P_{21}^{PSV}(z,0) &= \left(\frac{-i}{R(\omega)}\right)[Re(u_z(0,\omega))Im(u_z(z,\omega)) \\
&-Im(u_z(0,\omega))Re(u_z(z,\omega))],
\end{aligned}
$$

$$
\begin{aligned}
P_{22}^{PSV}(z,0) &= \left(\frac{1}{R(\omega)}\right)[Re(u_x(0,\omega))Re(u_z(z,\omega)) \\
&+Im(u_x(0,\omega))Im(u_z(z,\omega))]. \qquad \text{(B8)}
\end{aligned}
$$

where

$$
\begin{aligned}
R(\omega) &= Re(u_x(0,\omega))Re(u_z(0,\omega)) \\
&+ Im(u_x(0,\omega))Im(u_z(0,\omega)) \qquad \text{(B9)}
\end{aligned}
$$

Hence, the propagator matrix elements can be expressed in terms of displacements at the depth of interest z and at the free surface (z=0). For a layered medium, the propagator matrix in equation B6 can be obtained by combining the PSV and SH propagator matrices, each of which is the product of the corresponding propagator matrices for each of the layers. Even though the combination of the product matrix results in a different matrix, if each of the layers are homogeneous, it has the same form as shown in equation B6. Hence, the expressions in equation B8 gives the propagator matrix elements of the matrix obtained by combining the PSV and the SH matrix of the layered medium.